

**Probing the Alignment-Dependent Mechanical Behaviors
and Time-Evolutional Aligning Process of Collagen Scaffolds**

Journal:	<i>Journal of Materials Chemistry B</i>
Manuscript ID	TB-ART-06-2022-001360.R1
Article Type:	Paper
Date Submitted by the Author:	09-Aug-2022
Complete List of Authors:	Zhai, Chenxi; Cornell University Sullivan, Patrick; Northeastern University, Chemistry and Chemical Biology Martin, Cassandra; Northeastern University, Chemistry and Chemical Biology Shi, Haoyuan; Cornell University, Sibley School of Mechanical and Aerospace Engineering Deravi, Leila; Northeastern University, Chemistry and Chemical Biology Yeo, Jingjie; Cornell University, Sibley School of Mechanical and Aerospace Engineering;

Probing the Alignment-Dependent Mechanical Behaviors and Time-Evolutional Aligning Process of Collagen Scaffolds

Chenxi Zhai¹, Patrick A. Sullivan², Cassandra L. Martin², Haoyuan Shi¹, Leila F. Deravi², Jingjie Yeo^{1*}

¹² Lab for Engineering Living Materials, Sibley School of Mechanical and Aerospace Engineering, Cornell University, Ithaca, NY, 14853, USA.

²Department of Chemistry and Chemical Biology, Northeastern University, 360 Huntington Avenue, Boston, MA 02115, USA.

E-mail: jingjieyeo@cornell.edu

Abstract

Efficiently manipulating and reproducing the collagen (COL) alignment *in vitro* remains challenging because many of the fundamental mechanisms underlying and guiding the alignment process are not known. We reconcile experiments and coarse-grained molecular dynamics simulations to investigate the mechanical behaviors of a growing COL scaffold and assay how changes in fiber alignment and various cross-linking densities impact their alignment dynamics under shear flow. We find higher cross-link densities and alignment levels significantly enhance the apparent tensile/shear moduli and strength of a bulk COL system, suggesting potential measures to facilitate the design of stronger COL based materials. Since fibril alignment plays a key factor in scaffold mechanics, we next investigate the molecular mechanism behind fibril alignment with Couette flow by computationally investigating the effects of COL's structural properties such as chain lengths, number of chains, tethering conditions, and initial COL conformations to the COL's final alignment level. Our computations suggest that longer chain lengths, more chains, greater amounts of tethering, and initial anisotropic COL conformations benefit the final alignment, but the effect of chain lengths may be more dominant over other

factors. These results provide important parameters for consideration in manufacturing COL-based scaffolds where alignment and cross-linking are necessary for regulating performance.

KEYWORDS: collagen, scaffold, biomaterials, coarse-grained molecular dynamics, mechanical property

1. Introduction

Type I collagen (COL) is a scleroprotein^{1, 2} found in abundance within the connective tissues of almost all living systems. As the primary component of the extracellular matrix (ECM), COL contributes to physical³, chemical⁴, and mechanical functions^{5, 6}—all of which rely on the alignment of COL fibrils *in vivo*. These functions include stimulating cell interactions and maintaining structural stability in tissues and organs. Yet, efficiently controlling and reproducing COL alignment *in vitro* remains challenging because the mechanisms underlying its hierarchical alignment across multiple spatial scales is largely not known. While several techniques are available to induce and align COL fibrous networks *in vitro*, such as counter-rotating extrusion^{7, 8}, biaxial gel compression⁹, and magnetic bead-induced alignment^{10, 11}, they too suffer from challenges including complex pre- and post-processing steps, scalability, and ease of use. We recently designed and developed an alternative method to simultaneously polymerize and grow aligned COL fibers as scaffolds at the centimeter scale¹². This device consists of one rotating inner cylinder and another concentric, stationary outer cylinder.

This paper builds off our preliminary studies, where we showed that the Couette flow generated by the device aligns the COL fibrils during the natural polymerization process to form anisotropic COL scaffolds¹². We expand on this to provide further insight in the dynamic nature of the alignment process. Specifically, we investigate how the alignment of the fibrils quantitatively

affect the mechanical performance of the resulting COL scaffolds, and how efficient, high-quality alignment can be achieved theoretically. To do so, design parameters influencing the alignment of the COL scaffolds must be clearly defined, determined, then concretely connected to the mechanical properties of the aligned COL scaffolds. Greater insight into the aligning process will improve the effectiveness and efficiency of *in vitro* production to fully harness the remarkable properties of COL for a variety of engineering applications, such as designing bio-inspired materials for tissue engineering.

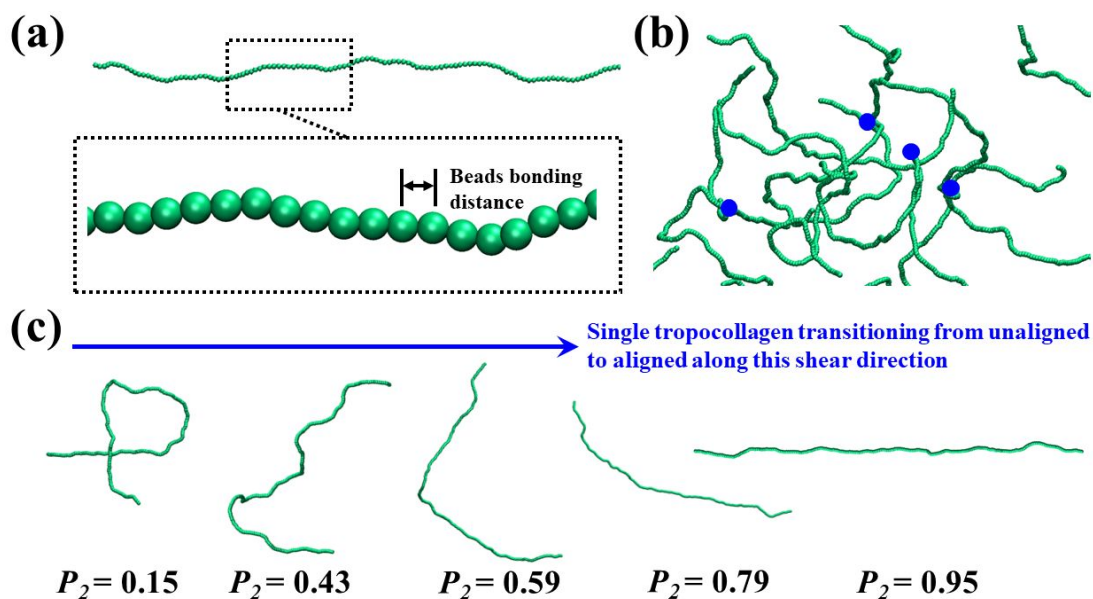


Figure 1. (a) The coarse-grained (CG) bead-spring model of single tropocollagen molecule. (b) The bulk simulated isotropic COL network with cross-links marked with blue points. (c) Simulation snapshots of the evolving conformation of a single tropocollagen from unaligned (left) to aligned (right) in the direction of the x -axis with the alignment degree characterized by P_2 (detailed in Results & Discussion and Computational Methods sections).

To address these challenges, we reconcile computational and *in vitro* experimental approaches to gain in-depth understanding of the alignment-dependent mechanical behaviors and the time-evolutional alignment process of bulk type I COL scaffold across multiple spatial scales. We use a well-developed coarse-grained molecular dynamics (CGMD) simulation framework¹³ (see SI and Methods), which is a bead-spring CG model with implicit solvents, described by multi-body

potentials that handle the fluid shear within the model (**Figure 1**). A cross-link is created between the terminal bead of a tropocollagen and that of an adjacent tropocollagen. The cross-link density spans from 0 to 80% in our study, where 100% cross-link density indicates the theoretical limit of having two terminal cross-links per tropocollagen (see Methods). We predict the tensile and shear behavior of the COL networks as a function of conformational alignment levels and cross-linking densities. We then experimentally investigate how aligning and cross-linking of bulk COL impact the mechanical properties of a scaffold, thereby facilitating future optimization of scaffold processing with experimentally-controllable parameters. Finally, differences in bulk COL networks' alignment over time are investigated computationally to identify critical factors that influence these differences. This integrative research significantly expands the computational design space for exploring mesoscale conformational dynamics of bio-inspired materials and informs experimental strategies for efficiently preparing highly aligned, fibrous COL networks *in vitro*.

2. Results & Discussion

2.1 Computational alignment-dependent mechanical behaviors of COL networks

We validate the accuracy and our implementation of this CGMD framework with uniaxial tensile tests and three-point bending tests of a single tropocollagen molecule (~308 nm in length) by comparing against existing literatures^{13, 14}. The computed mechanical properties agree reasonably well with previous findings^{13, 14}, supporting the predictability of this model. The details of this validation can be found in the Supporting Information (SI). The uniaxial tensile and shear behaviors of purely isotropic COL networks are then simulated as a function of the cross-link density¹⁵⁻¹⁷, ranging between 0% to 80%. The apparent tensile modulus of 5.5 kPa for 80% cross-

links in our CG model (**Figure 2(a)**) falls in the range from experiments¹⁸ and finite element models¹⁹ (1.5 kPa – 24.3 kPa). Differences can be primarily attributed to varying experimental and computational conditions such as cross-link densities and strain rates. More importantly, the apparent tensile moduli and ultimate strength of bulk isotropic COL networks increase as the cross-link density increases from 0 to 80%, where hyperelastic (rubber-like) behavior²⁰ can only be observed with cross-link densities at least above 60%. Only the apparent tensile modulus and ultimate stress before failure of the COL are compared here, fracture strains (strain where the bulk COL breaks or fails) of the tensile deformation of bulk COL are given in the SI (**Table S2**). Similarly, cross-linking density also strongly influences the shear behavior, where more cross-links lead to larger rigidity and ultimate shear strength (**Figure 2(c)**). A positive proportional relation is found between the cross-link density and apparent tensile/shear modulus/ultimate strength (**Figure 2(b)** and **(d)**). This relation resembles the trends found in previous studies of COL fibrils^{17, 21} but differs a little in the initial deformation stage. Our results show gradually increasing apparent tensile/shear moduli while previous studies^{17, 21} showed similar moduli at small strains, such as 0.1. This discrepancy likely arises because our model incorporates an isotropic COL network with uniformly distributed cross-links in contrast to highly anisotropic COL fibrils where collagen backbone stretching dominates during tensile deformation. For isotropic COL networks, stretching of both cross-links and molecular backbones collectively contribute to the tensile behavior. Interestingly, high cross-link densities in isotropic COL networks also result in secondary hyperelastic deformations, resembling the findings in aligned COL fibrils¹⁷.

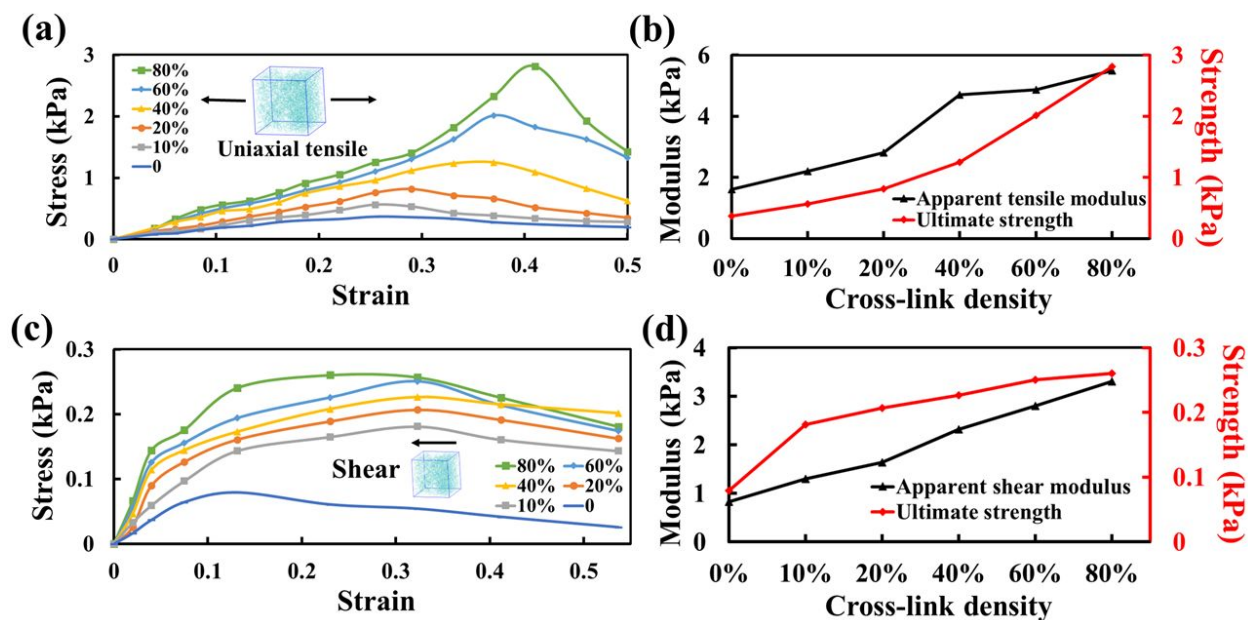


Figure 2. The computational stress-strain relation in (a) uniaxial tension and (c) shear for bulk isotropic COL scaffold under strain rates of $10^7/s$. The computational apparent (b) tensile and (d) shear modulus gradually increases as a function of increasing cross-link densities from 0 to 80%.

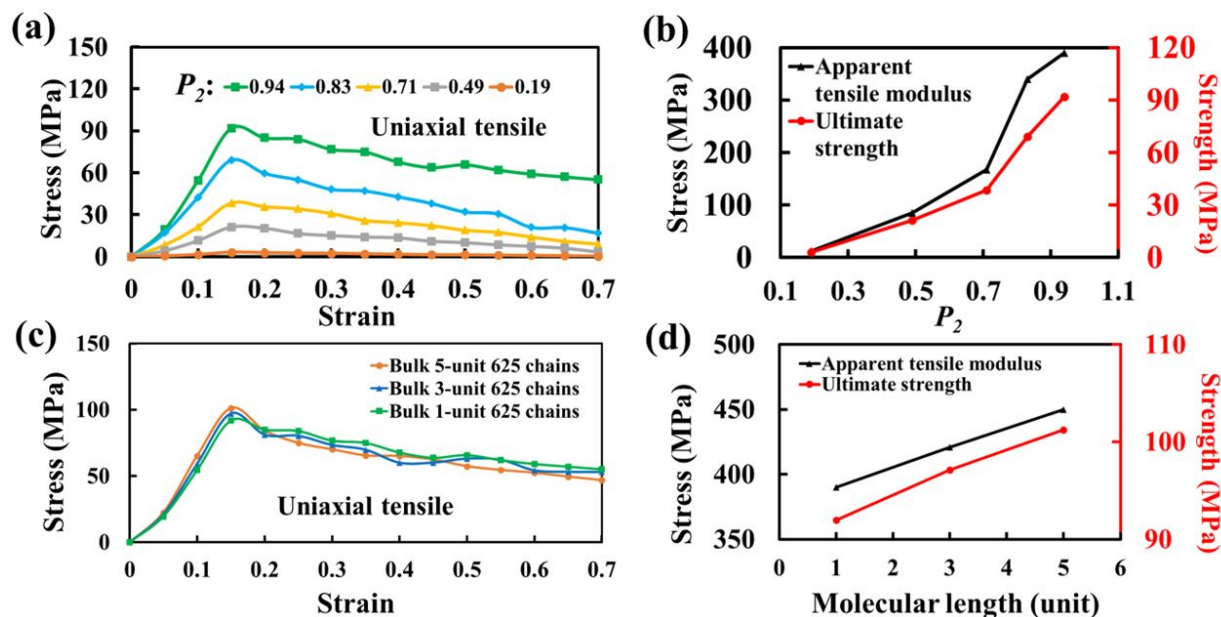


Figure 3. The computational stress-strain relation of the bulk COL networks under uniaxial tension with 80% cross-links and strain rates of $10^7/s$ having different (a) alignments and (c) molecular lengths. We use the nomenclature such that, for instance, a “5-unit 625 chains COL” consists of 625 COL oligomer chains and each oligomer chain consists of 5 connected repeating monomeric units. The computed apparent tensile modulus and ultimate strength gradually increase as a function of the (b) P_2 , and (d) molecular length.

To study the effects of the alignment on the mechanical properties of COL networks, we perform uniaxial tensile tests for several COL networks, ranging from fully isotropic to fully anisotropic

(i.e., with P_2 values of 0.19, 0.49, 0.71, 0.83, and 0.94). P_2 is an effective parameter to track the conformation of a series of connected particles that is used extensively^{12, 22-24} for measuring the alignment of polymer chains. It is a validated qualitative measure fluctuating between value of 1 (perfectly aligned) and value of 0 (perfectly disordered). If it is increasing over time until it reaches a plateau, this indicates that the chain becomes more aligned over time (see Computational Methods and SI for full details) and the plateau illustrates that equilibrium has been achieved. A vector, $\mathbf{e}_i = \frac{\mathbf{r}_{i+1} - \mathbf{r}_{i-1}}{|\mathbf{r}_{i+1} - \mathbf{r}_{i-1}|}$, is used to describe the local chain alignment at every bead, where \mathbf{r} is the chord vector connected to the bead i . Based on this vector, the orientational parameter $P_{2-force}$ can be derived along the direction of the applied force:

$$P_{2-force} = \frac{\sum_{i=1}^N 3((\mathbf{e}_i \cdot \mathbf{e}_{force})^2) - 1}{2N} \quad (1)$$

where N is the total number of beads, and \mathbf{e}_{force} is the unit vector in the direction of the applied force. We will refer to $P_{2-force}$ simply as P_2 for brevity.

The computed apparent tensile modulus of 0.39 GPa for the nearly aligned COL networks with 80% cross-links agrees well with previous computational models (0.4 – 0.5 GPa²⁵) but is significantly smaller than the values determined experimentally (2.2 – 3.5 GPa²⁶), possibly due to: (1) the cross-link densities can be assigned in the computations, while they are hard to measure in experiments; (2) strain rates have to be relatively high (10⁷/s) in computations due to computing power limit, while it is much lower in experiments. More importantly, the apparent tensile modulus and ultimate strength increase when P_2 increases, and the COL networks become more aligned (**Figure 3(a)**). Intuitively, the better mechanical robustness is due to more bonded cohesive interactions between beads carrying the uniaxial loads in the direction of the Couette flow (force direction in the simulation). In contrast, there are fewer bonded cohesive interactions for less aligned COL

networks along the uniaxial tensile loading direction. **Figure 3(b)** clearly depicts this positive relation between the apparent tensile modulus, ultimate strength, and P_2 . For an isotropic COL network which has a P_2 close to 0, the stresses are orders of magnitude smaller than networks with higher P_2 , hence the corresponding results are omitted for clarity.

We further investigate the effects of COL oligomer chain length to the uniaxial mechanical behavior for nearly aligned, bulk COL networks. With the increase of the COL oligomer chain length, a slightly higher apparent tensile modulus and ultimate strength are found (**Figure 3(c)**). The trends of the modulus and strength are highlighted in **Figure 3(d)**. Interestingly, a similar trend was found by Buehler and coworkers²⁷, where longer molecular lengths resulted in stronger COL fibrils. There are some slight differences because of the different cross-linking densities, chain numbers, and molecular lengths. Our computed apparent tensile modulus of bulk 5-unit-oligomer COL network (0.45 GPa) approximates the 0.4 – 0.5 GPa²⁵ and 2.2 – 3.5 GPa²⁶ found in literature, which may indicate that 5-unit-oligomer COL are sufficient for accurately predicting the mechanical behaviors of much longer COL fibrils in experiments. Our findings indicate that increasing COL molecular length strengthens the networks up to a limit of approximately 5 monomer units. Interestingly, this trend of the strength increasing initially followed by a plateau is in qualitatively agreement with previous findings²⁷ and thus further validates the our findings. The plateau was rationalized by the COL deformation transitioning from homogeneous shear to nucleation of slip pulses²⁷. We next perform mechanical tests on centimeter-scale COL scaffolds made with our device to confirm our predictions that cross-linking and alignment are critical in scaffold mechanics.

2.2 Experimental alignment-dependent mechanical behaviors of COL scaffolds

To expand on the results from the computational analysis, we next tested the mechanical properties of centimeter-scale scaffolds containing anisotropic or isotropic fibrillar COL using our Couette flow assembly platform. We prepared anisotropic and isotropic COL scaffolds (**Figure 4(a)**) to investigate how the alignment of the COL fibrils within the scaffolds impacts the maximum stress and the corresponding strain at rupture. We observe that the highly aligned scaffolds withstand a maximum stress of 0.368 ± 0.048 MPa before breaking, whereas the isotropic scaffolds have a maximum stress of 0.194 ± 0.045 MPa (**Figure 4(b)**, **Figure 4(c)**). In addition, the strains at rupture are $23.9 \pm 4.3\%$ and $15.2 \pm 4.1\%$ for the anisotropic scaffold and the isotropic scaffold, respectively (**Figure 4(c)**). These results suggest that the alignment of the fibrils in the scaffolds regulates both the load bearing capabilities and extensibility of the COL scaffold.

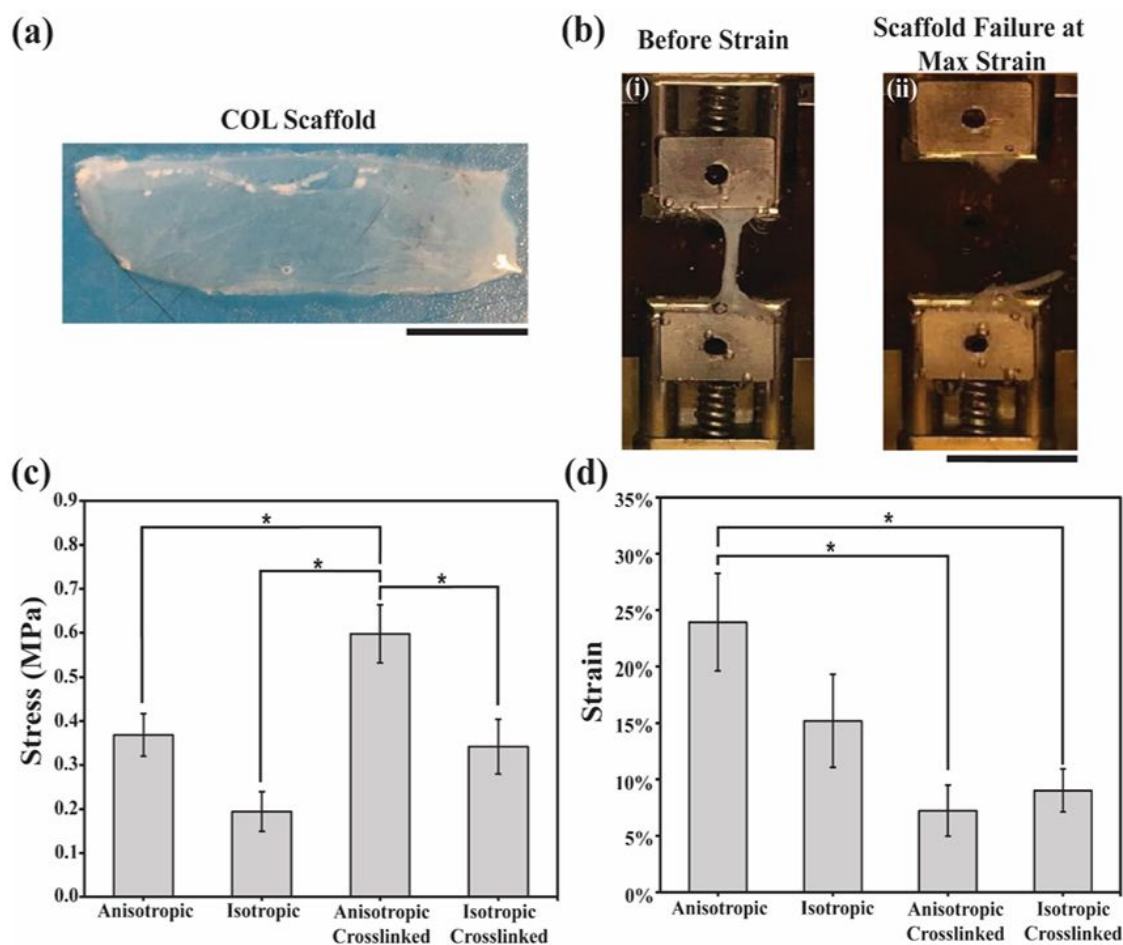


Figure 4. A comparison of the mechanical properties of the experimentally prepared non-crosslinked and crosslinked, anisotropic and isotropic COL scaffolds. Representative images of (a) isotropic COL scaffold prior to mechanical testing, (b) mechanical testing platform, where (i) the scaffold loaded in the clamps attached to the anchor point and the load cell and actuator before strain is applied and (ii) the scaffold post load to failure regime, resulting in a scaffold failure. (c) Experimental stresses at point of rupture for the four scaffold conditions over three independent scaffolds and error is reported as \pm standard deviation (SD). (d) Experimental strain (%) at the point of rupture for the four scaffold conditions over three independent samples and error is reported as \pm SD. Statistically significant for both sets of results are denoted with an asterisk where $p < 0.05$. Scale bars = 1 cm.

To investigate whether the presence of external crosslinks affects the mechanical properties of the COL scaffolds, the COL is crosslinked using a 2.5% glutaraldehyde solution. Glutaraldehyde chemically crosslinks COL fibrils at the amine groups, primarily on the lysines and hydroxylysines, present on the COL fibrils²⁸. At this percentage of crosslinks, we anticipate that

the fibrils with available amine groups have become modified to effectively alter the mechanical performance of COL. To test this, we monitor the maximum stress at rupture for both the anisotropic and isotropic scaffolds compared with their un-crosslinked counterparts. The crosslinked anisotropic and isotropic scaffolds have a maximum stress of 0.589 ± 0.066 MPa and 0.341 ± 0.062 MPa, respectively (**Figure 4(d)**), representing a 60% and 76% increase in the maximum stress compared with the non-crosslinked samples, respectively. There is also a change in the maximum stress between the crosslinked anisotropic and isotropic scaffolds, suggesting that altering alignment is overall more important in regulating mechanics than inducing glutaraldehyde crosslinking at this concentration. Crosslinking impacts the extensibility of the scaffolds, which is reduced to $7.2 \pm 2.3\%$ and $9 \pm 1.9\%$ for anisotropic and isotropic scaffolds, respectively (**Figure 4(d)**). These values are significantly lower compared with the non-crosslinked scaffolds for the anisotropic scaffold indicating a loss of elasticity and an increase in stiffening of COL, as the crosslinks are formed. Interestingly, the anisotropic and isotropic crosslinked scaffolds are not significantly different from one another, indicating that crosslinking impacts both scaffolds in a similar way, independent of alignment.

These experimental results differ from the computational results significantly in magnitude, which is expected due to the following two reasons. First, the strain rate in computations is $10^7/s$, owing to the scale limit of MD simulations, while it is only $\sim 2 \times 10^{-4}/s$ in experiments. Much smaller strain rates usually lead to smaller strength, strain, and toughness.^{13, 29} Second, the experimental crosslinking density is challenging to be quantified, which may be much smaller than the computational counterpart, finally leading to a much smaller stress than the computational 80%-cross-linked COL fibrils. This may also cause the lower fracture strain found in the experimental cross-linked COL

network. Nonetheless, the experimental findings still hold qualitative significance in comparison to the computational results: the experimental results correspond well with our computational prediction of the impacts of alignment and cross-links to the mechanical behaviors of bulk COL scaffold, i.e., the anisotropy and cross-links can significantly boost the strength and moduli of the bulk COL scaffold. Regardless, the deformation mechanisms observed in our experiments will require further in-depth investigation using other computational methods such as discrete fiber network models. Here, using DPD, we primarily reveal the underlying molecular-scale deformation mechanisms that regulate the dynamic alignment of COL and provide deeper insight for larger-scale experimental design to align COL *in vitro*. In the following paragraphs, we investigate possibly influential factors of the COL structural properties, such as COL fibril chain length, chain numbers, tethering condition, and COL initial conformation, that could affect the final COL alignment.

2.3 Influential Factors Regulating the Alignment of COL in a Scaffold

While our computational/experimental findings provide a framework to validate our approach, the mechanisms underlying the initial alignment process under Couette flow remains unknown. To test this, we study how multiple COL structural property parameters, such as COL fibril chain length (e.g, polymerization time), chain numbers (e.g., concentration), tethering (e.g., interfacial bonding during polymerization), and initial conformation, influence the alignment. When we create COL scaffolds under Couette flow¹², we use a rotating spindle that is coated with a uniform layer of gelatin to provide a surface to adhere/tether COL during fibrillogenesis. The spinning process itself involves multiple steps, wherein the COL monomer units first tether to the gelatin, then simultaneously polymerize and align under flow. The computational tethering force F here is

defined as a uniaxial anchoring force applied on a bead at one end of the oligomer; in this configuration, only the **initial** deformation of the COL oligomer subject to this tethering force F is simulated, which is defined as the uncoiling and alignment of the COL oligomer on the spindle¹⁴. The threshold tethering force $F = 0.05$ kcal/mol/Å for longer COL oligomer or 0.005 kcal/mol/Å for shorter COL oligomer is determined in our previous publication¹². A greater alignment is found for longer chain length, where the P_2 increases from ~ 0.6 to ~ 0.9 (**Figure 5(a) – (c)**). However, the rate of achieving the final alignment does not change much (~ 2 ns). These findings indicate that the COL fibril length does not accelerate the aligning process; nonetheless, it contributes to the final level of alignment. This is likely due to the larger total inter-monomer-unit repulsive, non-bonded interactions (**Table S3**), which facilitate the overall long-chain alignment.

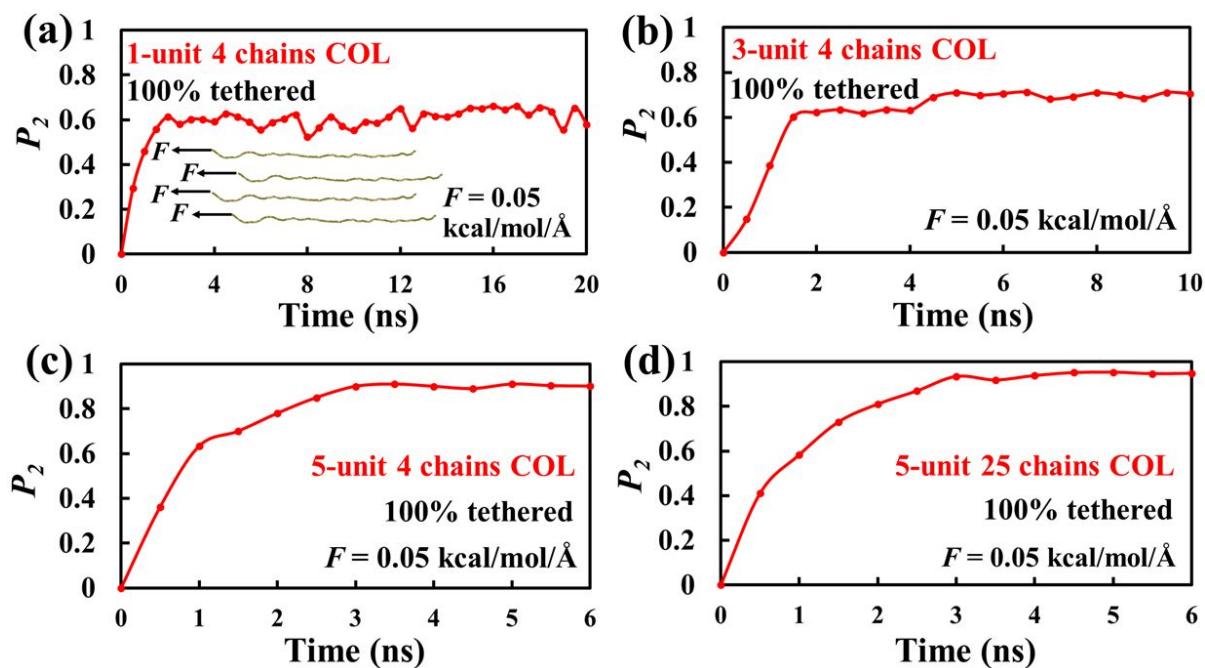


Figure 5. Computational evolution of P_2 over time and its relationship with COL chain lengths and numbers. There is greater alignment (P_2 approaching unity), but not faster alignment, when the chain length increases from 1- to 5-unit in (a), (b), and (c), and the COL chain number increases from 4 to 25 in (c) and (d).

To further demonstrate the COL chain length effects, 50%-tethered (50% of the total COL chains tethered) COL chain networks with different chain lengths are simulated (**Figure 6**) to compare

against 100%-tethered counterparts (**Figure 5**). Similarly, the alignment metric of P_2 gradually enhances from 0 to 0.6 as the chain length increases. More interestingly, less tethering even leads to a low P_2 value that is under 0.6, which shows the importance of tethering effects. This effect was also discussed in our previous paper¹². More importantly, we find that longer COL chain lengths can enable similar alignment with much fewer total chains and less tethering if a force equal to or above the previously-determined threshold force ($0.05 \text{ kcal/mol/\AA}$)¹² is applied, comparing **Figure 6(a)** against **Figure 5(a)**, **Figure 6(c)**, and **(d)**. These data suggest that longer COL chain length is also a major beneficial factor to facilitate the overall aligning of the COL network. Although a larger threshold magnitude of force is needed for longer-chain oligomers¹², the already-aligned portion of the chain may drive others (yet to be aligned COL) through bonding, by which the overall level of alignment is improved. Similarly, the COL chain numbers also have similar effects on the final level of alignment (**Figure 6(c)** and **(d)**), as demonstrated in detail in another study¹². In addition, even though the final alignment is greater for longer chain and more chain numbers, faster alignment is not observed, possibly owing to contradicting factors, such as more cohesive interactions between non-bonded beads in longer, more-chain system.

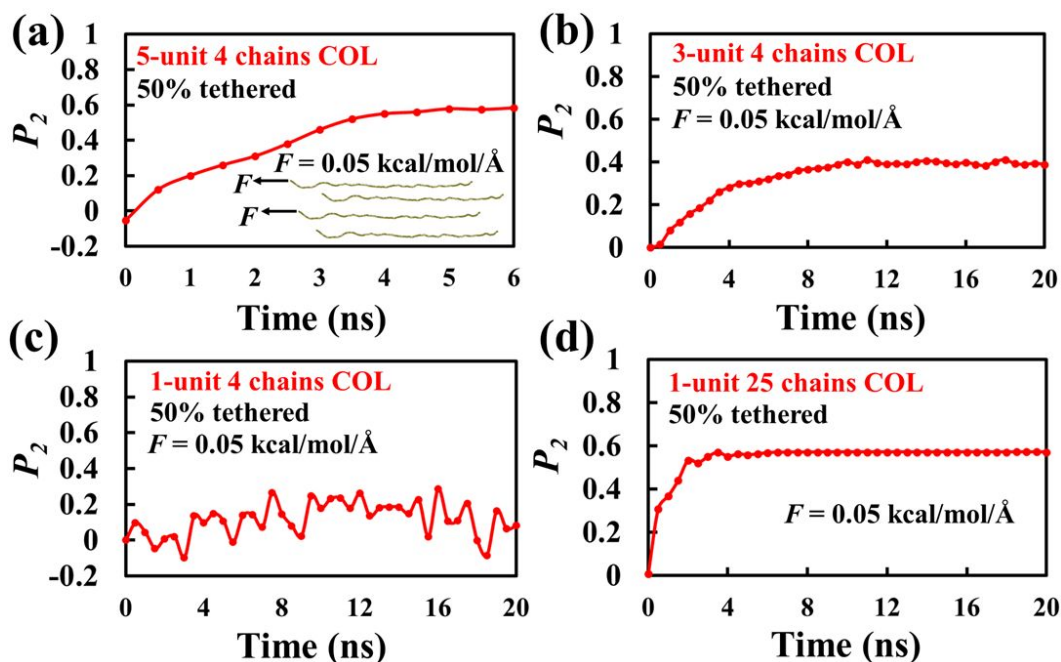


Figure 6. Computational time-dependent P_2 evolution and its relationship with COL chain length when 50% of the COL chains are tethered. The alignment is greater when the COL chain length increases from 1- to 5-unit in (c), (b), and (a). Longer COL is able to align with much fewer total chains and less tethering shown in **Figure 6(a)** by comparing against **Figure 5(a)**, **Figure 6(c)**, and (d).

The effects of initial conformation to the final alignment level are further investigated by comparing between starting from vertically aligned anisotropic conformation and from purely isotropic conformation. Interestingly, the 50%-tethered bulk COL network with a vertically-aligned anisotropic initial conformation takes much shorter time of ~ 2 ns to align (**Figure 7(a)** and (b)) compared to the 6 ns (100% tethering) or 70 ns (66% tethering) of the isotropic counterpart shown in our previous study¹². However, for single tropocollagen, **Figure 7(c)** shows a similar aligning time and level compared to starting from an isotropic structure¹², which indicates that the largely accelerated aligning for bulk COL network is only due to the interactions among COL monomer units, instead of the adjustment of each monomer unit itself.

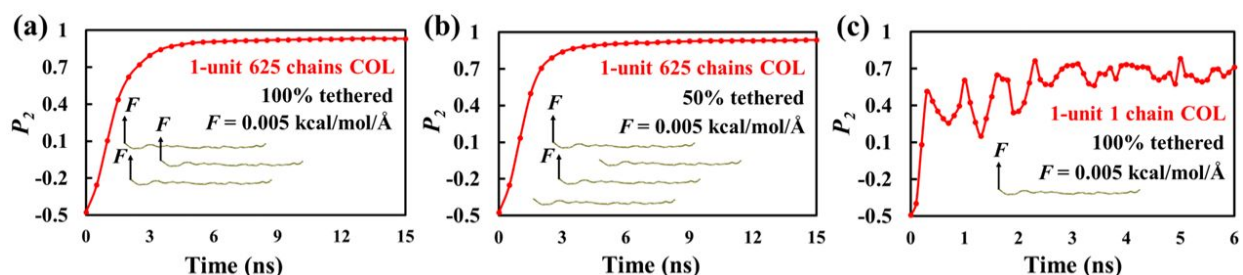


Figure 7. Computational time-dependent P_2 evolution where the shear starts from a vertically aligned anisotropic conformation. (c) shows no much difference between from isotropic and anisotropic structure for single tropocollagen, comparing to previous simulated results¹².

This speed discrepancy may be mainly attributed to the densely distributed repelling beads close to each other due to pair interactions and isotropy, which hinders the fast, effective diffusion of atoms in isotropic systems, whilst this is nonexistent in anisotropic systems. Recalling that different initial conformations also play an important role in the aligning, these properties suggest opportunities to design more cost-effective measures for facilitating alignment. In summary, we find that longer COL chain length, more COL chains, more tethering, and anisotropic initial conformations are favorable factors for facilitating a more effective and higher-level aligning.

3. Conclusion

This integrative computational and experimental study investigated the time-evolutional, alignment-dependent mechanical behaviors of type I COL scaffolds with different cross-link densities under shear flow, which is correlated with the formation and integration of COL in the scaffolds. With a well-validated bead-spring CGMD framework, we first simulated the uniaxial and shear behaviors of the bulk COL network as a function of cross-link densities and alignment levels, which corresponded with experimental findings in trends of the mechanical behaviors of the COL scaffold. The increasing cross-link densities (from 0 to 80%) and alignment (with P_2 values ranging from 0.19 to 0.94) significantly enhanced the uniaxial apparent tensile/shear

modulus and strength of COL. We then systematically investigated the effects of oligomer chain length, chain number, tethering, and initial conformations to the final alignment level of the tropocollagen and bulk COL. Longer chain lengths, more chains, more tethering, and initial anisotropic conformations promoted final alignment, but the chain lengths were the dominant factor. Through this study, we elucidated the initial aligning mechanism under the impact of several key theoretically variable parameters, thereby facilitating future optimization of collagen-based scaffold processing. This integrative research will inform new and existing experimental platforms that can simultaneously achieve scalability, reproducibility, and simplicity, thereby achieving high-performance alternatives to scaffold manufacturing techniques.

4. Computational Methods

An extensively developed mesoscale CGMD COL simulation framework^{13, 27} is used to simulate the collagen's alignment behavior under shear. This framework accurately captured the mechanical behavior of COL, from discrete molecules to fibrils^{13, 17, 30, 31}. This CG model was used to characterize multiple properties, e.g., tension^{13, 14, 17, 21, 27, 29, 32}, shear^{13, 27}, compression²⁷, and cross-link-related properties^{17, 21} of COL molecules and bundles. These properties for macromolecules³³ are conventionally challenging to be simulated via all-atomistic (AA) models, necessitating the general development of CG models³⁴⁻³⁷ for polymers, which effectively and reasonably handle the task in a predictive and versatile manner. This CG model is derived from a higher-fidelity AA triple helical tropocollagen model, which is generated from Protein Data Bank entry 3HR2 type I COL³⁸, in order to access larger time and length scales (see SI for full details)¹³. The solvated tropocollagen molecules are modeled with beads (pseudo-atoms), which correspond to 10 – 20 atoms for each bead, and connective springs that are 14 Å long at equilibrium between two connected beads. Periodic boundary conditions (PBC) are set to approximate a bulk system.

The simulation box is set longer than a tropocollagen molecule to avoid end-to-end interactions of a same molecular chain because of PBC.

The multi-body potential interactions between beads consist of paired, bonded, and angular potentials in this CG simulation framework. The pair interactions are described with a Lennard-Jones (LJ) style potential:

$$E_{paired} = 4\epsilon_{LJ} \left[\left(\frac{\sigma_{LJ}}{r} \right)^{12} - \left(\frac{\sigma_{LJ}}{r} \right)^6 \right] \quad (2)$$

where $\sigma_{LJ} = 14.72 \text{ \AA}$ is the interactive beads equilibrium distance between the two interacting beads where the LJ potential energy is zero, and $\epsilon_{LJ} = 11.06 \text{ Kcal/mol}$ is the dispersion energy. The bonded interactions are described as:

$$E_{bonded} = \begin{cases} k_1(r - r_0)^2, & r < r_1 \\ k_2(r - r_0)^2, & r_{break} > r > r_1 \\ 0, & r > r_{break} \end{cases} \quad (3)$$

where $k_1 = 17.13 \text{ kcal/mol/\AA}^2$, $k_2 = 97.66 \text{ kcal/mol/\AA}^2$ are the bond stiffness under small and large strains, $r_0 = 14 \text{ \AA}$ is the equilibrium bonding distance, $r_1 = 18.2 \text{ \AA}$ is the critical bonding distance for large strains, and $r_{break} = 21 \text{ \AA}$ is the bond breaking distance. The angular potential is described as:

$$E_{angular} = k_{angular} [\beta - \beta_0]^2 \quad (4)$$

where $k_{angular} = 14.98 \text{ kcal/mol/rad}^2$ is the angular bending stiffness and β_0 is the equilibrium angles ranging from 170° to 180° . This forcefield and associated parameters are derived from AA models and are validated in SI, our previous work¹², and a number of publications^{13, 14, 21, 27}. We create chemical covalent bonds between side chains of the residues of two tropocollagen molecules to form cross-links¹⁷, mimicking the intermolecular enzymatic cross-links primarily developed between lysine or hydroxylysine residues at the ends of tropocollagen molecules^{15, 16}. A divalent

cross-link is assumed to link two different tropocollagens. A cross-link is created between the last bead of a tropocollagen and one adjacent tropocollagen based on a distance criterion ($< 14.68\text{\AA}$). The cross-link density spans from 0 to 80% in our study. An 100% cross-link density indicates two terminal cross-links per tropocollagen, which is the maximum number of cross-links that can form per tropocollagen¹⁵. The distribution of the cross-links in the COL is created randomly. The full table of parameters are given in **Table S1**. The fluid shear is handled within this implicit-solvent model, where the tethering is handled by applying a point force on one bead at one end of the tropocollagen mimicking the experimental starting condition, in which a single tropocollagen adheres/tethers to gelatin during spinning (see SI for full details).

The local chain alignment at each bead i is described using vectors $\mathbf{e}_i = \frac{\mathbf{r}_{i+1} - \mathbf{r}_{i-1}}{|\mathbf{r}_{i+1} - \mathbf{r}_{i-1}|}$. Correspondingly, an alignment parameter P_2 is used to describe the orientation of the chain along the shearing direction:

$$P_2 = \frac{\sum_{i=1}^N 3\langle (\mathbf{e}_i \cdot \mathbf{e}_{shear})^2 \rangle - 1}{2N} \quad (5)$$

where \mathbf{e}_{shear} is the unit vector along the shear direction and N is the total number of beads (see SI for full details)^{22, 23}. The COL networks are equilibrated for 2 ns before the shear and run with shear for long enough time until P_2 fluctuates around a certain value. All the simulations are run with the NVT ensemble³⁹. The visualization of the molecular morphology is realized by the VMD software (<http://www.ks.uiuc.edu/Research/vmd/>)⁴⁰. The apparent tensile modulus is computed as:

$$E = \frac{stress}{strain} \quad (6)$$

where the stress and strain data are picked up from the elastic deformation region.

5. Experimental Methods

Generating Anisotropic and Isotropic Scaffolds

Anisotropic and isotropic scaffolds were generated using a custom-built device with a rotating inner cylinder (the spindle) and a stationary outer cylinder (the reservoir) as detailed in our previous report¹². The spindle was first coated with a uniform layer of 10% w/v gelatin (9000-70-8, Electron Microscopy Sciences) to create a uniformly thin sacrificial layer that aids in the tethering and ultimate release of COL. Next, acid solubilized monomeric bovine type I COL (5026-1KIT, Advanced Biomatrix) was prepared with final concentration of 2.5 mg/mL COL at pH 7.3 ± 0.1 using phosphate buffered saline (PBS) and transferred immediately to the protein reservoir of the device, where the spindle was spun at 75 s^{-1} (103 rpm) for 15 minutes. Afterwards the spindle was raised and removed from the reservoir and the reservoir was then cleaned to ensure all excess COL was removed from the bottom of the reservoir. This process of adding the COL solution was repeated four more times to build the aligned COL scaffolds for testing. After this, the spindle was removed from the device and a vertical incision was made down the scaffold. The spindle was then submerged in a heated 1x PBS bath to dissolve the sacrificial layer of gelatin and remove the scaffold.

To create the isotropic COL scaffolds, the same procedure was carried out but with the difference of a three-minute delay prior to the start of spinning. Crosslinking of the COL scaffolds was done with a 2.5% glutaraldehyde solution in 1x PBS for 2 hours. Glutaraldehyde was chosen as the crosslinker due to its prevalence in tissue fixation to aid in imaging. Glutaraldehyde works as a crosslinker by interacting with the amine groups of lysine and hydroxylysine and has long been used to crosslink collagenous materials, and at concentrations higher than 0.2%, complete

crosslinking can be seen⁴¹. We used a variation of this protocol for preparing tissue samples for TEM for our crosslinking⁴². Briefly, our scaffolds were immersed in 2 mL of 2.5 w/v% glutaraldehyde (16120, Electron Microscopy Sciences) in 1x PBS for 2 hours to ensure complete crosslinking, after which the glutaraldehyde was removed through a graded series of solution exchanges with 1x PBS.

To determine the crosslinking density of the COL scaffolds we looked at the ratio of glutaraldehyde to COL triple helix. Assuming that we have 100% COL incorporation, we anticipate all 7.5 mg of COL present in the scaffold. Using the mass of a collagen triple helix from A. Sorushanova et al.⁴³ as 300,000 Da, we calculated that there are 1.51×10^{16} triple helices present in the scaffold. As we used 2.5% w/v glutaraldehyde and used 2 mL in our crosslinking solution, we calculated that there is 0.05 g of glutaraldehyde present and that corresponds to 0.0005 mol of glutaraldehyde in our system. Using Avogadro's number, we found that there are 3.01×10^{20} glutaraldehyde molecules, and this corresponds to a ratio of 19,976 glutaraldehyde molecules for every triple helix. At this ratio we can assume that there is complete crosslinking of the COL scaffold based on previous observations⁴¹.

Measurement of the Cross-Sectional Area of the COL Scaffolds

The thickness of the scaffold was determined by using a light microscope (Eclipse Ti2, Nikon). The scaffold was placed flat, 0.1 mm thick glass coverslip (Warner Instruments) and then excess moisture was removed to prevent floating of the scaffold over the glass surface. Next, we analyzed the thickness of the scaffolds with a z-scan carried out on the light microscope, where the bottom of the glass coverslip represented the "bottom" layer and the top of the scaffold indented with a

glass capillary denoted the “top” layer. We adjusted the glass at both the bottom and top positions to create a focal contrast point to ensure that the focal plane was distinguishable. At the end of each recording, the thickness of the glass substrate was subtracted from the total, where the difference represented the full thickness of the scaffold in hydrated conditions. Five measurements were reported along the upper, middle, and lower portion of the scaffold in the 3 cm direction for a total of fifteen measurements per scaffold. Together with the measured length and width of each scaffold, the thickness measurements allowed for the calculation of the cross-sectional area of the scaffold, based on the assumption that the scaffolds were uniform in thickness. This was repeated for every sample and used to collect the corresponding mechanical data, corresponding to 3 samples for each of the 4 conditions. Error is standard deviation over the different scaffolds’ average thickness. Through this analysis we determined that for the non-crosslinked COL scaffolds had a thickness of $12.93 \pm 2.88 \mu\text{m}$ for the aligned scaffold and $27.67 \pm 1.29 \mu\text{m}$ for the unaligned scaffold. For the crosslinked scaffolds we observed a thickness of $10.87 \pm 3.50 \mu\text{m}$ for the aligned scaffold and $35.43 \pm 5.60 \mu\text{m}$ for the unaligned scaffold. We tested 3 samples for thicknesses and determined the standard deviation.

Mechanical Testing

Stress/strain curves for each scaffold were generated using a custom built uniaxial tensile tester which consisted of a PI M-230.25 High Resolution Linear Actuator with DC and Stepper Motor with a Model 31 Load Cell (Honeywell). The force exerted was tracked and controlled with the MTESTQuattro Controller (Admet). Prior to analysis, the scaffold was removed from solution and loaded into the custom-built clamps. There, the anchor points were reinforced with 2 μL of VetBond (3M) to help prevent any slippage during the experiment. This glue was allowed to dry

for eight minutes, after which point, the chamber was filled with 1x PBS to rehydrate the scaffold. The scaffold was then left to sit for another eight minutes to ensure that it was fully hydrated in the buffered solution. The mechanical test regime was carried out as a strain to failure, which consisted of a linear ramp at a rate of 0.005 mm/sec until the load was 0.005N to remove any slack in the material followed by a pull rate of 0.01mm/sec until failure. Mechanical testing was carried out with 3 samples each for the four conditions.

Data Analysis of the Mechanical Test Results

Data is presented as the average \pm the standard deviation of the results. Statistical significance of the stress and percent strain between the conditions is determined via a one-way ANOVA test where $p < 0.05$. If any results are significantly different, a Tukey test was performed to calculate which conditions were different from each other.

Declarations

Ethics approval and consent to participate

Not applicable

Consent for publication

Not applicable

Availability of data and materials

The data supporting the findings of this study are available from the corresponding author upon request.

Competing interests

The authors declare that they have no competing interests

Funding

US National Science Foundation (Grant No. 2038057)

Author Contributions

C.Z., H. S., and J.Y. designed, performed, and analyzed the computational experiments. P.S., C.L.M., P.A.S., and L.F.D. designed both the device and experiments and interpreted the results. P.A.S. and C.L.M. performed the experiments and analyzed the results. All authors made the figures and wrote the manuscript.

Acknowledgements

C.Z., H.S., and J.Y. acknowledges support provided by the XSEDE program under Grant TG-BIO210063 and MAT200004. J.Y. acknowledges support from the US National Science Foundation (Grant No. 2038057) and Cornell University's faculty startup grant.

References

1. L. Andreotti, D. Cammelli, A. Bussotti and P. Arcangeli, in *Biochemistry, Pathology and Genetics of Pulmonary Emphysema*, Elsevier, 1981, pp. 83-90.
2. X.-D. Chen, *A Roadmap to Nonhematopoietic Stem Cell-based Therapeutics: From the Bench to the Clinic*, Academic Press, 2018.
3. C. Doillon, M. A. Watsky, M. Hakim, J. Wang, R. Munger, N. Laycock, R. Osborne and M. Griffith, *The International journal of artificial organs*, 2003, **26**, 764-773.
4. B. León-Mancilla, M. Araiza-Téllez, J. Flores-Flores and M. Piña-Barba, *Journal of applied research and technology*, 2016, **14**, 77-85.
5. H. Shi, L. Zhao, C. Zhai and J. Yeo, *Chemical Communications*, 2021.
6. J. Chen, T. Ahn, I. D. Colón-Bernal, J. Kim and M. M. Banaszak Holl, *ACS nano*, 2017, **11**, 10665-10671.
7. S. Yang, X. Shi, X. Li, J. Wang, Y. Wang and Y. Luo, *Biomaterials*, 2019, **207**, 61-75.
8. H. R. Hoogenkamp, G.-J. Bakker, L. Wolf, P. Suurs, B. Dunnewind, S. Barbut, P. Friedl, T. H. Van Kuppevelt and W. F. Daamen, *Acta biomaterialia*, 2015, **12**, 113-121.

9. J. L. Zitnay, S. P. Reese, G. Tran, N. Farhang, R. D. Bowles and J. A. Weiss, *Acta biomaterialia*, 2018, **65**, 76-87.
10. C. Guo and L. J. Kaufman, *Biomaterials*, 2007, **28**, 1105-1114.
11. M. Antman-Passig and O. Shefi, *Nano letters*, 2016, **16**, 2567-2573.
12. C. L. Martin, C. Zhai, J. A. Paten, J. Yeo and L. F. Deravi, *ACS Biomaterials Science & Engineering*, 2021, DOI: 10.1021/acsbmaterials.1c00566.
13. M. J. Buehler, *Journal of Materials Research*, 2006, **21**, 1947-1961.
14. M. J. Buehler and S. Y. Wong, *Biophysical journal*, 2007, **93**, 37-43.
15. D. R. Eyre and J.-J. Wu, *Collagen*, 2005, 207-229.
16. S. Viguet-Carrin, P. Garnero and P. Delmas, *Osteoporosis international*, 2006, **17**, 319-336.
17. B. Depalle, Z. Qin, S. J. Shefelbine and M. J. Buehler, *Journal of the mechanical behavior of biomedical materials*, 2015, **52**, 1-13.
18. B. A. Roeder, K. Kokini, J. E. Sturgis, J. P. Robinson and S. L. Voytik-Harbin, *Journal of biomechanical engineering*, 2002, **124**, 214-222.
19. T. Stylianopoulos and V. H. Barocas, *Computer methods in applied mechanics and engineering*, 2007, **196**, 2981-2990.
20. V. R. Sherman, W. Yang and M. A. Meyers, *Journal of the mechanical behavior of biomedical materials*, 2015, **52**, 22-50.
21. M. J. Buehler, *Journal of the mechanical behavior of biomedical materials*, 2008, **1**, 59-67.
22. C. Yong and P. Higgs, *Macromolecules*, 1999, **32**, 5062-5071.
23. J. Liu and R. Yang, *Physical Review B*, 2010, **81**, 174122.
24. S. Lin, Z. Cai, Y. Wang, L. Zhao and C. Zhai, *npj Computational Materials*, 2019, **5**, 1-12.
25. S. Eppell, B. Smith, H. Kahn and R. Ballarini, *Journal of the Royal Society Interface*, 2006, **3**, 117-121.
26. R. B. Svensson, H. Mulder, V. Kovanen and S. P. Magnusson, *Biophysical journal*, 2013, **104**, 2476-2484.
27. M. J. Buehler, *Proceedings of the National Academy of Sciences*, 2006, **103**, 12285-12290.

28. L. D. Olde Damink, P.; Van Luyn, M.; Van Wachem, P.; Nieuwenhuis, P.; Feijen, J, *J. Mater. Sci. Mater. Med.* , 1995, **6**, 460–472
29. A. Gautieri, M. J. Buehler and A. Redaelli, *Journal of the Mechanical Behavior of Biomedical Materials*, 2009, **2**, 130-137.
30. A. Gautieri, A. Russo, S. Vesentini, A. Redaelli and M. J. Buehler, *Journal of Chemical Theory and Computation*, 2010, **6**, 1210-1218.
31. N. Zhang, Y. Cheng, X. Hu and J. Yeo, *Current Opinion in Chemical Engineering*, 2019, **24**, 79-87.
32. B. Depalle, Z. Qin, S. J. Shefelbine and M. J. Buehler, *Journal of Bone and Mineral Research*, 2016, **31**, 380-390.
33. Y. Qiu, C. Zhai, L. Chen, X. Liu and J. Yeo, *ACS Biomaterials Science & Engineering*, 2021.
34. C. Zhai, H. Zhou, T. Gao, L. Zhao and S. Lin, *Macromolecules*, 2018, **51**, 4471-4483.
35. C. Zhai, S. Lin, M. Wang, H. Zhou, E. Stanisauskis, Z. Cai, J. Yeo and W. Oates, *Advanced Functional Materials*, 2021, 2104414.
36. C. Zhai, T. Li, H. Shi and J. Yeo, *Journal of Materials Chemistry B*, 2020.
37. J. Yeo, W. Huang, A. Tarakanova, Y.-W. Zhang, D. L. Kaplan and M. J. Buehler, *Journal of Materials Chemistry B*, 2018, **6**, 3727-3734.
38. J. P. Orgel, T. C. Irving, A. Miller and T. J. Wess, *Proceedings of the National Academy of Sciences*, 2006, **103**, 9001-9005.
39. M. P. Allen and D. J. Tildesley, *Computer simulation of liquids*, Oxford university press, 2017.
40. W. Humphrey, A. Dalke and K. Schulten, *Journal of molecular graphics*, 1996, **14**, 33-38.
41. M.-T. Sheu, J.-C. Huang, G.-C. Yeh and H.-O. Ho, *Biomaterials*, 2001, **22**, 1713-1719.
42. L. Graham and J. M. Orenstein, *Nature protocols*, 2007, **2**, 2439-2450.
43. A. Sorushanova, L. M. Delgado, Z. Wu, N. Shologu, A. Kshirsagar, R. Raghunath, A. M. Mullen, Y. Bayon, A. Pandit and M. Raghunath, *Advanced materials*, 2019, **31**, 1801651.